9

Super-Resolution Microscopy: Interference and Pattern Techniques

Udo Birk [1,2,3], Gerrit Best [3,4], Roman Amberger [3], and Christoph Cremer [1,2,3]

[1] Institute of Molecular Biology GmbH (IMB), Ackermannweg 4, 55128 Mainz, Germany

[2] Mainz University, Department of Physics, Mathematics and Computer Science, Institute of Physics, Staudingerweg 9, 55128 Mainz, Germany

[3] Heidelberg University, Applied Optics and Information Processing, Kirchhoff-Institute for Physics, Im Neuenheimer Feld 227, 69120 Heidelberg, Germany

[4] Heidelberg University Hospital, Department of Ophthalmology, Im Neuenheimer Feld 400, 69120 Heidelberg, Germany

9.1 Introduction

In many scientific fields such as biology, medicine, and material sciences, microscopy has become a major analytical tool. Electron microscopy (EM) with nanometer resolution, on one hand, and light microscopy with a broad applicability, on the other, have allowed groundbreaking scientific achievements. Even though EM delivers unmatched resolution, light microscopy has never lost its relevance. Because of the vast popularity of fluorescent labeling techniques in recent years, the method of fluorescence microscopy has actually become one of the most important imaging techniques in the life sciences.

However, the intrinsically limited resolution of standard fluorescence microscopy compared to EM and X-ray microscopy is still a major drawback, as many biological specimens are of a size in the nanometer to micrometer range. Therefore, the standard light-microscopic resolution defined by Rayleigh [1] (Chapter 2) is often not sufficient to resolve the objects of interest.

Over the last years, different techniques, such as super-resolution fluorescence microscopy, have been established to compensate for the deficiency of low spatial resolution. These approaches use fluorescence excitation because this allows – in combination with other techniques – access to high-resolution object information.

These super-resolution methods (i.e., 4Pi [2–5], stimulated emission depletion (STED) (Chapter 10), structured illumination microscopy/patterned excitation microscopy (SIM/PEM) [6, 7], and localization methods (Chapter 8)) seemingly break the conventional resolution limit. However, it should be noted that the fundamental resolution limit is not broken directly. The super-resolution methods are based on conditions that are different from the assumptions of Rayleigh. Rayleigh's conclusions for self-luminous (i.e., fluorescent) objects do not consider

spatial or temporal variations of the light intensity. Basically, all super-resolution techniques depend on juggling with fluorescence excitation or emission.

In this chapter, we describe in detail two widefield methods that apply interference of the excitation light to make high-resolution object information accessible. These are structured illumination microscopy (SIM) (also referred to as *patterned excitation microscopy*, PEM) and spatially modulated illumination (SMI).

9.1.1   Review: The Resolution Limit

Regarding imaging systems, it is obvious that the rendering power (i.e., the capability to transmit structural information) is always limited to some degree. To describe the rendering power of an imaging system, the term *resolution* is employed. However, this term is ambiguously used, and there exist different scientific definitions for the resolving power of a system.

A commonly used resolution measure is the definition provided by Lord Rayleigh, which is described in Chapter 2. Rayleigh's definition is based on the point spread function (PSF) of an optical system (Section 2.3.3).

The PSF resembles the image of an ideal point-like object. The Rayleigh distance defining the resolution is the lateral distance between the maximum and the closest zero of the PSF.

It is given by

$$d_{\mathrm{Rayleigh}} = 0.61 \frac{\lambda}{n \sin \alpha} \tag{9.1}$$

When the PSF is the same for every position in the object plane, every point of the object is broadened by the same PSF. This is a reasonable approximation in many microscopy applications. It may be helpful to imagine the microscope as an artist who draws an image representation of the object with a brush; fine details of the object will be visible only if the artist uses a tiny brush, that is, a small PSF. Mathematically, this imaging process of drawing an image $A'(x,y)$ from an object $A(x,y)$ using the PSF as a brush can be represented by a convolution:

$$A'(x, y) = A(x, y) \otimes \mathrm{PSF}(x, y) \tag{9.2}$$

In Chapter 2, the optical transfer function (OTF) was introduced. The OTF is the Fourier transform (FT) of the PSF:

$$\mathrm{FT}[\mathrm{PSF}(x, y)] = \mathrm{OTF}(k_x, k_y) \tag{9.3}$$

The convolution theorem states that convolution in position space corresponds to multiplication in frequency space, and vice versa. Here and in the following, "frequency" denotes *spatial frequency*, that is, a modulation along the spatial coordinates. Hence, by applying the FT to the image $A'(x,y)$ and the object $A(x,y)$, we can describe the imaging process (Eq. (9.2)) as a multiplication:

$$\mathrm{FT}[A'] = \mathrm{FT}[A] \times \mathrm{OTF} \tag{9.4}$$

The PSF is band-limited, which means that the OTF is zero for high frequencies beyond a cut-off frequency $k_{\mathrm{cut\text{-}off}}$:

$$\mathrm{OTF}(\mathbf{k}) = 0 \quad \text{for } |\mathbf{k}| \geq k_{\mathrm{cut\text{-}off}} \tag{9.5}$$

All object information beyond this cut-off frequency is filtered out by the multiplication with the OTF and is therefore missing in the image. The lack of high
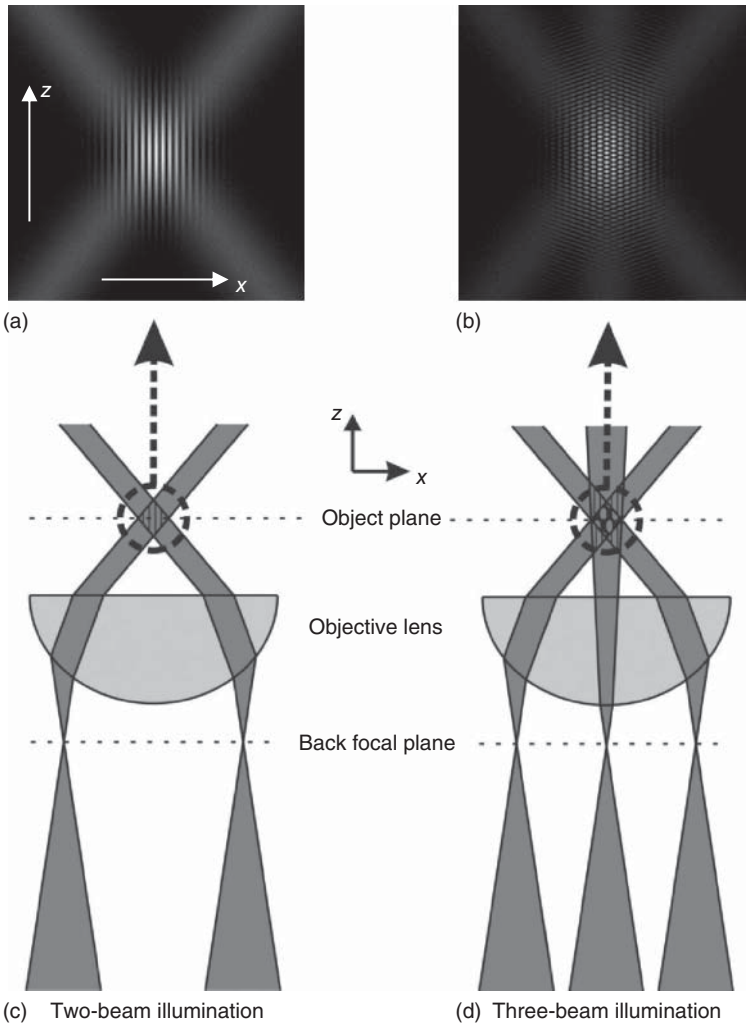
Figure 9.1 Cut-off frequency of an OTF. The supported frequency region of a conventional microscope is a toroid. For small lateral frequency components k_x and k_y, the axial component k_z of the cut-off frequency approaches zero. This represents the so-called missing cone.

frequencies in the image is the reason for the limited resolution. In Figure 9.1, the cut-off frequency is shown in three dimensions.

The cut-off frequency can be used as a measure for the resolution of an optical system, as an alternative to the Rayleigh criterion.

A definition of resolution referring to the object's frequency is that of Abbe [8]. Abbe considered a fine grating placed on a microscope. The finest, yet resolvable pattern (with grating distance d_{Abbe}) would define the resolution of the microscope. Calculation yields

$$d_{Abbe} = \frac{\lambda}{2n \sin \alpha} \tag{9.6}$$

The corresponding maximum transmittable frequency (i.e., cut-off frequency) is given by $k_{cut\text{-}off} = 2\pi/d_{Abbe}$.

In our case, both definitions ($d_{Rayleigh}$ and d_{Abbe}) are analogous and yield similar values. In the following paragraphs, ways to circumvent this resolution limit are discussed, which are based on manipulations of the illumination conditions.

9.2 Structured Illumination Microscopy (SIM)

In SIM, the object is illuminated with a periodic illumination pattern. This pattern is used in order to manipulate the object's spatial frequencies [6, 7], as described in the following sections. In SIM, the pattern is usually projected through the objective lens, and no additional devices or mechanisms are used to illuminate the object from the opposite side.

In practice, the pattern is generated by interference of a number of coherent beams proceeding from the objective lens and meeting in the object plane (Figure 9.2).

The periodic pattern can be of arbitrary shape, but typically the modulation of the pattern is only one dimensional in the focal plane (x–y plane), as is the case with the patterns shown in Figure 9.2. Two methods to spatially modulate the excitation intensity in SIM are common: two-beam interference, also called *fringe projection*, and three-beam interference, the so-called grid projection. Examples for optical setups generating the coherent beams are given in Section 9.2.6.

(a)

(b)

(c) Two-beam illumination

(d) Three-beam illumination

Figure 9.2 Illumination path in structured illumination microscopy. (a) Lateral interference pattern when two coherent beams are used for illumination, as shown in (c). (b) In case of interference of three beams, as shown in (d), the modulation is two dimensional (lateral and axial direction, e.g., along x- and z-axis).

In a typical three-beam interference SIM setup, the coherent beams are arranged in a symmetrical configuration as follows: one light beam propagates along the optical axis, and two beams span an angle with the first beam. One of the other beams propagates at an angle α with respect to the optical axis and the other one at the angle $-\alpha$. All three beams span a common plane (interferometer plane). The resulting interference pattern has a modulation along one direction in the focal plane and also a modulation along the optical axis.

The other method works with only two beams (Figure 9.2a) and corresponds to the three-beam case with a blocked central beam along the optical axis. The

corresponding interference pattern exhibits only a modulation along the focal plane (x–y plane).

In the following, the image formation process and the consequent resolution improvement of SIM will be shown using the simpler method of two-beam interference.

9.2.1 Image Generation in Structured Illumination Microscopy

In this section, a mathematical description of the image generation process in SIM is developed.

As mentioned in Section 9.1.1 and in Chapter 2, the imaging process of a widefield microscope can be described by

$$A'(x, y) = A(x, y) \otimes \mathrm{PSF}(x, y) \tag{9.7}$$

where A' is the image and A is the object. The object A is the distribution of the emitted fluorescence light in the object plane. The PSF is the impulse response, blurring the image.

When fluorescence saturation is insignificant (under usual fluorescence microscopy conditions), the object distribution is proportional to the illumination intensity $I_{\mathrm{ill}}(x, y)$ and the fluorophore distribution $\rho(x, y)$:

$$A(x, y) = \rho(x, y) \times I_{\mathrm{ill}}(x, y) \tag{9.8}$$

In conventional widefield microscopy, the illumination intensity is constant and the object is essentially the fluorophore density.

In SIM, however, the illumination is spatially varying and this variation is carried through to the image. For the case of two-beam illumination (Figure 9.2a), the illumination distribution is given by

$$I_{\mathrm{ill}}(x, y) = I_0[1 + m\cos(k_{\mathrm{G}x}x + k_{\mathrm{G}y}y + \phi)] \tag{9.9}$$

or in vector notation with the position vector **r**

$$I_{\mathrm{ill}}(\mathbf{r}) = I_0[1 + m\cos(\mathbf{k}_{\mathrm{G}}\mathbf{r} + \phi)] = (1 - m)I_0 + 2\,m\,I_0\,\cos^2(\mathbf{k}_{\mathrm{G}}\mathbf{r}/2 + \phi/2) \tag{9.10}$$

The modulation strength m is a scalar value between 0 and 1. For $m = 1$, the distribution has a minimum of zero and a maximum of $2I_0$. The intensity modulation takes place in the x–y plane. To express the modulation in the 2D space, the **k**-vector of the grating $\mathbf{k}_{\mathrm{G}}$, with $|\mathbf{k}_{\mathrm{G}}| = 2\pi/G_{\mathrm{SIM}}$, is used, where the grating constant G_{SIM} is the spatial period of the modulation. $\mathbf{k}_{\mathrm{G}}$ points in the direction of the modulation, that is, it is perpendicular to the stripes of the pattern and points along the object plane. The lateral position of the illumination pattern is determined by the phase φ.

Substituting Eq. (9.8) in Eq. (9.7) yields

$$A'(\mathbf{r}) = [\rho(\mathbf{r}) \times I_{\mathrm{ill}}(\mathbf{r})] \otimes \mathrm{PSF}(\mathbf{r}) \tag{9.11}$$

Now, the image information $\tilde{A}'$ in the frequency space is described by

$$\tilde{A}' = \mathrm{FT}[A'] = \mathrm{FT}[\rho \times I_{\mathrm{ill}}] \times \mathrm{OTF} \tag{9.12}$$

The multiplication of ρ and I_{ill} transforms into a convolution because of the convolution theorem:

$$\tilde{A}' = \tilde{\rho} \otimes \tilde{I}_{\text{ill}} \times \text{OTF} \tag{9.13}$$

This convolution of the FTs $\tilde{\rho}$ with $\tilde{I}_{\text{ill}}$ leads to a mixing of spatial frequencies and ultimately to a potentially enhanced optical resolution, as will be shown for the case of two-beam interference in the following. The FT of the illumination pattern (Eq. (9.10)) is

$$\tilde{I}_{\text{ill}}(\mathbf{k}) = \frac{1}{2\pi} \iint I_0 [1 + m \cos(\mathbf{k}_G \mathbf{r} + \phi)] e^{-i(\mathbf{kr})} \, d\mathbf{r} \tag{9.14}$$

Using the identity

$$\cos x = \frac{1}{2}(e^{ix} + e^{-ix}) \tag{9.15}$$

FT(I_{ill}) becomes

$$\tilde{I}_{\text{ill}}(\mathbf{k}) = \frac{1}{2\pi} \iint I_0 \left[1 + \frac{m}{2} e^{i(\mathbf{k}_G \mathbf{r} + \phi)} + \frac{m}{2} e^{-i(\mathbf{k}_G \mathbf{r} + \phi)} \right] e^{-i(\mathbf{kr})} \, d\mathbf{r} \tag{9.16}$$

Expanding this equation yields

$$\tilde{I}_{\text{ill}}(\mathbf{k}) = \frac{1}{2\pi} \iint I_0 \left(e^{-i\mathbf{kr}} + \frac{m}{2} e^{-i(\mathbf{kr} - \mathbf{k}_G \mathbf{r})} e^{i\phi} + \frac{m}{2} e^{-i(\mathbf{kr} + \mathbf{k}_G \mathbf{r})} e^{-i\phi} \right) d\mathbf{r} \tag{9.17}$$

With the Dirac delta distribution in exponential form

$$\delta(\mathbf{k} - \mathbf{a}) = \frac{1}{2\pi} \iint e^{i(\mathbf{xk} - \mathbf{xa})} \, d\mathbf{x} \tag{9.18}$$

the FT of the illumination pattern becomes a sum of delta functions with complex prefactors depending on ϕ:

$$\tilde{I}_{\text{ill}}(\mathbf{k}) = 2\pi \times I_0 \times \left[\delta(\mathbf{k}) + \frac{m}{2} e^{i\phi} \delta(\mathbf{k} - \mathbf{k}_G) + \frac{m}{2} e^{-i\phi} \delta(\mathbf{k} + \mathbf{k}_G) \right] \tag{9.19}$$

One delta function is located at the origin (corresponding in principle to the conventional fluorescence imaging case) and the other two are at the reciprocal period of the illumination pattern.

In the Fourier-transformed image $\tilde{A}'(\mathbf{k})$, the convolution of these delta functions with the Fourier-transformed object distribution $\tilde{\rho}(\mathbf{k})$ leads to a sum of copies of the object information shifted by the positions of the delta functions. Each copy is multiplied by its corresponding complex coefficient:

$$\tilde{A}'(\mathbf{k}) = \text{OTF}(\mathbf{k}) \times I_0 \frac{1}{\sqrt{2\pi}} \times \left[\tilde{\rho}(\mathbf{k}) + \frac{m}{2} e^{i\phi} \tilde{\rho}(\mathbf{k} - \mathbf{k}_G) + \frac{m}{2} e^{-i\phi} \tilde{\rho}(\mathbf{k} + \mathbf{k}_G) \right] \tag{9.20}$$

How far the single additional copies are shifted in the frequency space is defined by the angle of incidence α and the wave vector $\mathbf{k}$ of the incident light waves.

Note the low-pass filter property of the OTF (during image formation, the OTF is multiplied by FT[$\rho \times I_{\text{ill}}$]). As the frequencies of the additional copies of the image are shifted, a frequency region of previously irresolvable frequencies

beyond the cut-off limit $k_{\text{cut-off}}$ of these copies is shifted into the passband of the OTF. This frequency information is superposed with the information of the other copies and located in the frequency region imaged by the microscope. Therefore, it has to be separated and shifted back to its appropriate position after image acquisition. The separation and reconstruction process will be discussed in Section 9.2.2.

In case it is possible to separate the superimposed, that is, added frequency information copies in the acquired image, the additional copies can be shifted back to their original high spatial frequency position. It is apparent that now the frequency region of the image spans further in the direction of the modulation of the illumination pattern compared to the original image. Therefore, the resolution has been enhanced by this process, as higher frequency information is transmitted into the image. The factor of resolution improvement is given by the factor by which the size of the frequency region of the image is expanded.

The size of the resulting frequency region depends on the period of the illumination pattern. To calculate the maximum possible resolution improvement by SIM, the minimum possible grating distance should be considered. For illumination through the objective lens, the minimum grating distance is reached when the two incident coherent excitation beams with the vacuum wavelength $\lambda_{0\text{ex}}$ span the maximum angle, that is, illumination along the maximum opening angle of the acceptance cone of the objective lens. Therefore, the minimum grating distance is given by

$$G_{\text{SIMmin}} = \frac{\lambda_{0\text{ex}}}{2n\sin(\alpha_{\text{max}})} = \frac{\lambda_{0\text{ex}}}{2\text{NA}} = d_{\text{Abbe}} \tag{9.21}$$

which is the Abbe definition for the minimum grating distance of a yet-resolvable grating in the object plane for transmitted light microscopy.

In fluorescence microscopy, the wavelength of the emission light is close to that of the excitation light ($\lambda_{\text{em}} \approx \lambda_{\text{ex}}$). Hence, the reciprocal grating period of the smallest possible illumination pattern approximates the cut-off frequency $k_{\text{cut-off}}$. The delta functions of the Fourier-transformed illumination pattern are located at the positions $-2\pi/G_{\text{SIM}}$ and $+2\pi/G_{\text{SIM}}$. Therefore, the origins of the copies of Fourier-transformed information are shifted to the cut-off limit (Figure 9.3b). When these copies are separated and shifted back, the region of accessible information in the frequency space is twice as large as in the standard microscopy case. Thus, the resolution improvement in linear SIM can reach a factor of 2.

The term *linear* is used because in this case the dependence of the fluorescence emission intensity is considered to be linearly proportional to the excitation intensity.

Under usual microscopy conditions, saturation and photobleaching effects can be often be neglected, and the assumption of linear dependence of the fluorescence response on the excitation intensity holds true. Saturation and photobleaching effects would result in a decreasing gradient of the emission response with increasing excitation intensity. It has been shown [9, 10] that this nonlinear effect can be used to increase the resolution of SIM beyond the factor of 2 when the magnitude of the nonlinearity is maximized by the application of appropriate setup conditions such as, for example, special fluorochromes and
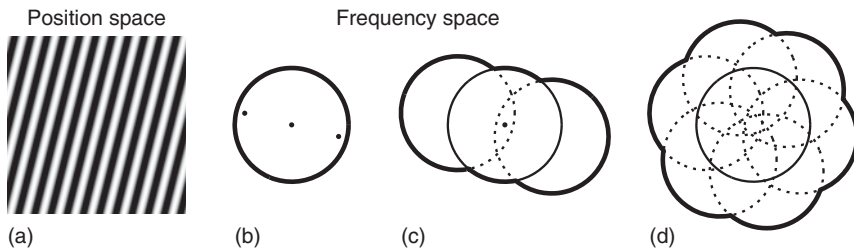
Figure 9.3 Accessible frequency region by SIM. The illumination pattern (a) contains three delta peaks in the frequency space as illustrated in the Fourier-transformed raw image (b). The circular area corresponds to the passband of the objective lens, that is, the bold outline shows the frequency limit. The raw data (b) consists of superposed original image information positioned at three different origins. After separation, the information can be shifted back to its respective position, resulting in an expanded accessible frequency area (c). To expand the resolution in the object plane not only along one direction but also isotropically, the illumination pattern is subsequently rotated to carry out the image acquisition with several illumination pattern orientations (d).

matched excitation intensities. In this case, the effective fluorescence emission pattern that is obtained from the fluorochrome distribution would contain the periodic illumination intensity pattern (Figure 9.3) and additionally higher harmonics of the fundamental pattern (not shown). In the frequency space, the higher harmonics shift the image information by twofold, threefold, or more of the shift by the fundamental pattern.

The twofold resolution improvement in linear SIM yields a lateral resolution of ~100 nm [11], whereas widefield and confocal microscopy can achieve ~230 and ~180 nm lateral resolution, respectively [12].

However, when an illumination pattern with modulation in only one direction in the optical plane (i.e., the plane of focus) is used, the resolution improvement is anisotropic and only maximum in the direction of the modulation (Figure 9.3c). To attain a more isotropic resolution, the direction of the modulation has to be applied in several directions in the optical plane (Figure 9.3d).

An alternative depictive approach to understand the resolution enhancing effect provided by SIM is to consider the Moiré effect, as shown in Figure 9.4. When two fine gratings are superposed, a third coarse grating with a larger spatial period (or grating distance) G_3 occurs. If one of the fine original patterns with a spatial period G_1 and also the resulting pattern is known, while the second fine grating with G_2 is unknown, the unknown pattern can be reconstructed mathematically.

The known and the unknown fine gratings represent the SIM excitation pattern and the high-frequency object information, respectively, whereas the coarse grating represents the detected image.

9.2.2 Extracting the High-Resolution Information

When structured illumination is applied, the total spatial frequency information transmitted through the objective lens increases. However, the additional information is overlaid with the original image information, as described in Section 9.2.1.

Figure 9.4 Moiré effect. If two fine patterns are superposed, a third, raw pattern, can occur.
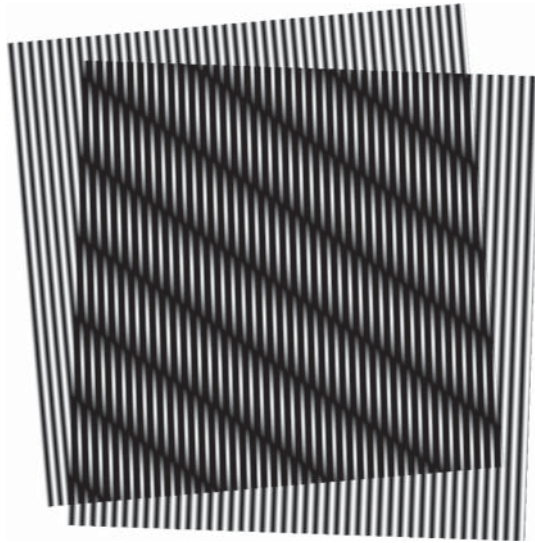
The additional information, therefore, has to be separated and shifted to the correct position in the frequency space. To separate the components, the acquisition of several images with different positions (phase ϕ, see Eq. (9.10)) of the illumination pattern is required. By this method, the complex coefficients (1, $(m/2)e^{i\phi}$, and $(m/2)e^{-i\phi}$) of the image copies depending on the grating position ϕ (see Eq. (9.20)) can be calculated for the different grating positions consecutively. The image information belonging to the single copies can be separated afterward by the respective coefficient. When using two-beam interference, three images with different grating positions are sufficient to solve the equations; for three-beam interference, five images are necessary.

After separation, the copies of the image information can be shifted to their correct position by the reciprocal vectors of the illumination grating. When the correctly processed information of the different copies is added, the resulting image has a higher resolution as compared to the original image.

As described previously, the resolution improvement in the focal plane is anisotropic if the modulation of the illumination pattern is one dimensional in the lateral direction.

In order to achieve an almost isotropic resolution improvement, nonetheless, in this case, a series of images are taken at different angles of the periodic illumination pattern, typically at 0°, 60°, and 120° (Figure 9.3d) or at 0°, 45°, 90°, and 135°.

It is also mathematically possible to use a two-dimensional (2D) grating producing a hexagonal pattern to generate the diffraction orders of the excitation light.

9.2.3 Optical Sectioning by SIM

Not only the lateral resolution, as shown in the 2D example in the previous paragraph, is improved in SIM compared to standard widefield microscopy but also the confocality can be improved, resulting in an optical section with less signal from the out-of-focus region.

This effect becomes clear when the widefield OTF (Figure 9.1) is considered. For the spatial frequencies k_x, $k_y = 0$, and $k_z \neq 0$, the OTF is always zero. A cone-shaped frequency region around the optical axis frequencies k_z in the OTF is missing. The corresponding information is not transmitted by the microscope. This "missing cone" problem results in the fact that in conventional microscopy the z-resolution is not well defined.

As shown in Figure 9.5, the additional object information copies provided by SIM are capable of covering the missing cone of the original OTF, and therefore yield an improved optical sectioning power of SIM compared to conventional fluorescence microscopy. However, in the case of two-beam illumination (Figures 9.2a,c and 9.5a,c), confocality is improved only if the illumination pattern frequency is (slightly) smaller than the cut-off frequency. At the cut-off, the missing cones overlap and therefore remain uncovered.

As is the case with lateral resolution, it is difficult to quantify the axial resolution of a microscope and it is important to find a suitable model to calculate or measure comparable quantitative values for different microscopy methods. For example, the full width at half-maximum (FWHM) of the 3D PSF in the axial dimension could be used. However, this z-direction FWHM depends on the x and y positions (Figures 2.12 and 9.12).

In the work of Karadaglić and Wilson [13], the optical sectioning powers of two different SIM setups and of a confocal microscope were compared using a model of a thin, fluorescent sheet located in the focal plane. The ability to determine the z position of the sheet by the microscopes was compared.

It was shown that both two-beam interference (fringe projection) and three-beam interference (grid projection) SIM exhibit optical sectioning strengths comparable to that of a confocal microscope. However, the three-beam interference provided a better optical sectioning capability compared to two-beam interference. Nevertheless, two-beam interference requires the acquisition of single images at three different phase positions as opposed to five different phase positions for three-beam interference, and because fewer object information copies are used, it is less susceptible to noise in the raw data.

The answer to the question whether two- or three-beam illumination is ultimately more favorable depends on the specimen that is analyzed. Two-beam
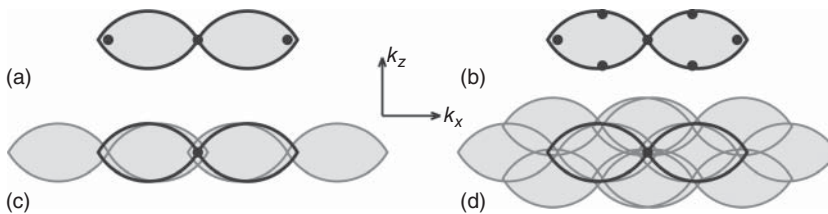

Figure 9.5 Resulting OTF in (a, c) two- and (b, d) three-beam illumination. The black spots in the microscope's widefield OTFs (a: two-beam and b: three-beam) show the origins of the shifted object information copies. When these copies are shifted back (c, d) to their correct positions, the effective OTF increases in size. The black outline shows the original widefield OTF cut-off border. The borders of the shifted OTFs are shown in gray. The corresponding illumination patterns are shown in Figure 9.2a,b.

interference is often used in cases where sectioning is achieved by other means, for example, via total internal reflection fluorescence illumination, or when the specimens are thin.

9.2.4 How the Illumination Pattern is Generated?

For structured illumination, a multitude of coherent light beams is necessary to generate the illumination conditions shown in Figure 9.2.

Basically, two techniques have been developed to arrange this: the application of a diffraction grating (Figure 9.6a), or the use of an interferometer (Figure 9.6b). In Section 9.2.6, examples for both approaches are shown.
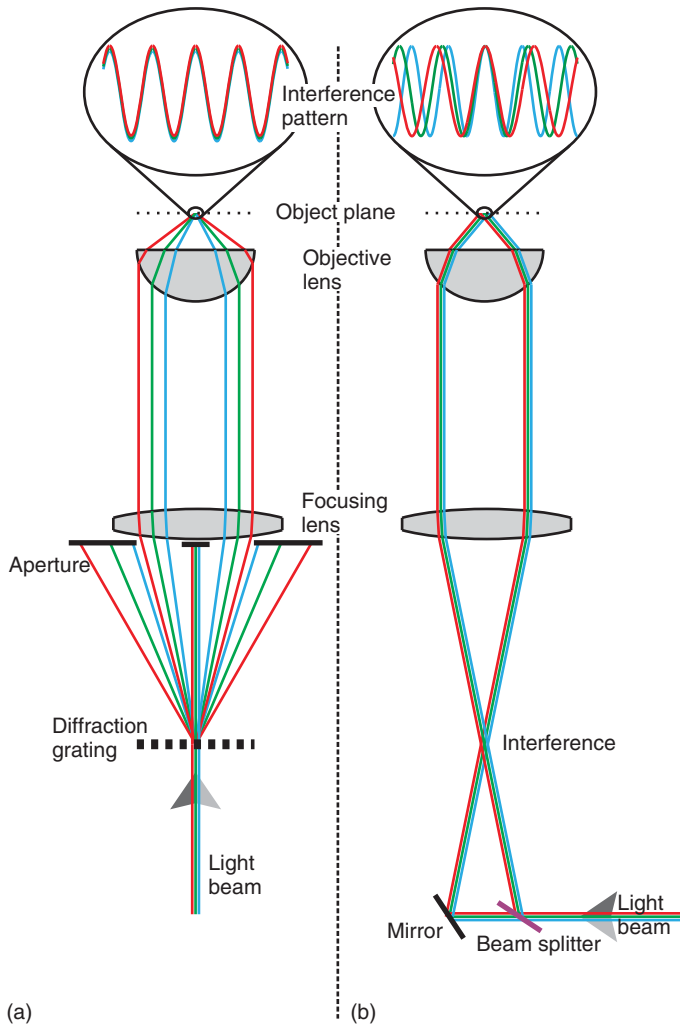
Figure 9.6 Beam path and interference pattern for (a) grating and (b) interferometer setup. In the grating setup shown here, the zero order of diffraction is blocked. Higher orders [±2, ±3, etc.] also do not enter the objective lens.

The two techniques differ in the dependence between the period of the illumination pattern and the wavelength of the excitation light (Figure 9.6).

In setups applying a diffraction grating in a conjugate image plane, an image of the grating is projected into the object plane. Therefore, the spatial period of the illumination pattern is independent of the wavelength of the illumination light. Hence, the illumination light does not need to be coherent. An incoherent light source (e.g., gas discharge lamp or light-emitting diode (LED)) can be used instead of a laser.

For an interferometer setup, on the other hand, the illumination pattern has a period proportional to the wavelength of light. The larger the wavelength, the coarser the pattern. Here, the light source has to be coherent in order to achieve a periodic intensity pattern (Figure 9.6b). For interferometer setups, the angle of the excitation light beams depends only on the angle of the interferometer. If this angle is set to a suitable value according to the objective lens's numerical aperture (NA) once, a change in interference angle is not necessary for different excitation wavelengths. For diffraction grating setups, a change in grating might be necessary if the excitation wavelength is changed. As shown in Figure 9.6a, the red beams hit the objective lens at the utmost border, whereas the blue beams are closer toward the center of the objective lens.

9.2.5 Mathematical Derivation of the Interference Pattern

In the equations for the illumination pattern (Eq. (9.9)) and the derived statements, a variable modulation strength m was used.

In order to explore the magnitude of the modulation strength, the interference pattern for a two-beam interference SIM setup is calculated in the following. The two initial beams are considered to be equally strong and have identical linear polarization $\mathbf{p}_0$. The right beam has a phase shift φ compared to the left beam.

In the following, the complex exponential form for the superposing waves is used instead of the trigonometric form. Both beams propagate identically along the z-direction before passing through the objective lens. While doing this, the left beam is tilted by the angle α and the right beam by $-\alpha$ (Figure 9.7) around the y-axis, thereby affecting the polarization of the beams.

Before passing through the lens, the electric fields of the left and the right beam are given by

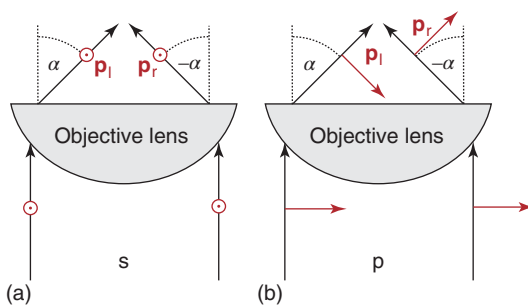$$\mathbf{E}_{l0} = \mathbf{p}_0 E_0 e^{i(\mathbf{k}_0 \mathbf{r} - \omega t)} \tag{9.22}$$

Figure 9.7 Polarization of the beams before and after passing through the objective lens for polarization (a) perpendicular (s) and (b) parallel (p) to the interferometer plane.

and

$$\mathbf{E}_{r0} = \mathbf{p}_0 E_0 e^{i(\mathbf{k}_0\mathbf{r} - \omega t - \phi)} \tag{9.23}$$

The polarization vector is a unity vector ($|\mathbf{p}_0| = 1$) pointing in the direction in which the electric field oscillates.

The original wave vector $\mathbf{k}_0$ points along the z-direction:

$$\mathbf{k}_0 = \begin{pmatrix} 0 \\ 0 \\ 1 \end{pmatrix} \frac{2\pi}{\lambda} \tag{9.24}$$

Behind the lens, the rotated polarizations of the beams are given by

$$\mathbf{p}_l = R_y(\alpha)\mathbf{p}_0 = \begin{pmatrix} \cos\alpha & 0 & \sin\alpha \\ 0 & 1 & 0 \\ -\sin\alpha & 0 & \cos\alpha \end{pmatrix} \mathbf{p}_0 \tag{9.25}$$

and

$$\mathbf{p}_r = R_y(-\alpha)\mathbf{p}_0 = \begin{pmatrix} \cos\alpha & 0 & -\sin\alpha \\ 0 & 1 & 0 \\ \sin\alpha & 0 & \cos\alpha \end{pmatrix} \mathbf{p}_0 \tag{9.26}$$

through application of the rotation matrix R_y around the y-axis.

The same rotation accounts for the wave vectors, which yields

$$\mathbf{k}_l = \begin{pmatrix} \sin\alpha \\ 0 \\ \cos\alpha \end{pmatrix} \frac{2\pi}{\lambda} \tag{9.27}$$

$$\mathbf{k}_r = \begin{pmatrix} -\sin\alpha \\ 0 \\ \cos\alpha \end{pmatrix} \frac{2\pi}{\lambda} \tag{9.28}$$

$$\mathbf{E}_l = \mathbf{p}_l E_0 e^{i(\mathbf{k}_l\mathbf{r} - \omega t)} \tag{9.29}$$

$$\mathbf{E}_r = \mathbf{p}_r E_0 e^{i(\mathbf{k}_r\mathbf{r} - \omega t - \phi)} \tag{9.30}$$

The superposition $\mathbf{E}_s = \mathbf{E}_l + \mathbf{E}_r$ in the object plane yields

$$\mathbf{E}_s = E_0(\mathbf{p}_l e^{i(\mathbf{k}_l\mathbf{r} - \omega t)} + \mathbf{p}_r e^{i(\mathbf{k}_r\mathbf{r} - \omega t - \phi)}) \tag{9.31}$$

The intensity is proportional to the absolute square of the electric field:

$$I \propto |\mathbf{E}_s|^2 \Rightarrow I = a|\mathbf{E}_s|^2 = a\mathbf{E}_s\mathbf{E}_s^* \tag{9.32}$$

with the proportionality constant a. By substituting Eq. (9.31) in Eq. (9.32), the intensity becomes

$$I = 2aE_0^2(1 + \mathbf{p}_l\mathbf{p}_r \cos[(\mathbf{k}_l - \mathbf{k}_r)\mathbf{r} + \phi]) \tag{9.33}$$

after some rearrangements. Substituting the wave vectors $\mathbf{k}_l$ and $\mathbf{k}_r$ (Eqs (9.27) and (9.28)) yields

$$I = 2aE_0^2 \left(1 + \mathbf{p}_l\mathbf{p}_r \cos\left[\frac{4\pi\sin\alpha}{\lambda}x + \phi\right]\right) \tag{9.34}$$

Obviously, with $\mathbf{p}_l\mathbf{p}_r = m$ and $2aE_0^2 = I_0$, the term is identical to the illumination pattern of a two-beam interference SIM microscope (Eq. (9.9)).

When both interfering beams of a two-beam interference SIM setup are equally strong, the modulation strength depends on the primary polarization of the beams and on the angle α by which the beams are deflected by the objective. To examine these effects, we compare two extreme cases of linear polarization: polarization perpendicular (s)

$$\mathbf{p}_{0s} = \begin{pmatrix} 0 \\ 1 \\ 0 \end{pmatrix}$$

to the interferometer plane and parallel (p)

$$\mathbf{p}_{0p} = \begin{pmatrix} 1 \\ 0 \\ 0 \end{pmatrix}$$

to the interferometer plane (Figure 9.7). The interferometer plane is the plane that is spanned by the two beams.

If the polarization of the incoming beams is perpendicular (s), the polarization of the single beams ($\mathbf{p}_l, \mathbf{p}_r$) will not be changed by passing through the objective lens (application of $R_y(\alpha)$ and $R_y(-\alpha)$) and the modulation m is unity (Figure 9.8a). For beams that are polarized parallel (p) to the interferometer plane, owing to the change in beam angle, the polarization of the left beam is rotated by α and of the right by $-\alpha$. For p polarization and $\alpha = 45°$, the polarizations and therefore the electric fields of both beams are perpendicular. The modulation strength $m = \mathbf{p}_l\mathbf{p}_r$ becomes zero and the resulting intensity of the object plane becomes constant (Figure 9.8b). Usually, the interferometer plane is rotated to different angles (usually 0°, 60°, and 120°) around the optical axis in the SIM image acquisition process. To achieve high modulation strength for all angles, the polarization of the excitation light has to be rotated with the pattern to allow s polarization in every case. This can be done, for example, with a rotatable half-wave plate or an electro-optic modulator.

9.2.6 Examples for SIM Setups

In SIM, the excitation intensity in the focal plane is a periodic pattern. To achieve this illumination distribution, different setups have been established. Commonly, the excitation light is projected through the same objective lens that is used for the detection of the fluorescence in order to generate a standing wave field, even though other illumination techniques with the use of additional optical devices or even near-field excitation are possible.

Most commonly, SIM microscopes use either a physical grating [6, 7] or a synthetic grating generated by a spatial light modulator (SLM) [14, 15] in an intermediate image plane to create the modulated pattern in the object plane (Figure 9.9).

Grating-based SIM is usually set up in such a way that only up to the ± first-order diffracted beams enter the objective lens. The use of higher orders (five and more beam interference) is possible but would lead to a more complicated separation of the copies of the Fourier-transformed object information
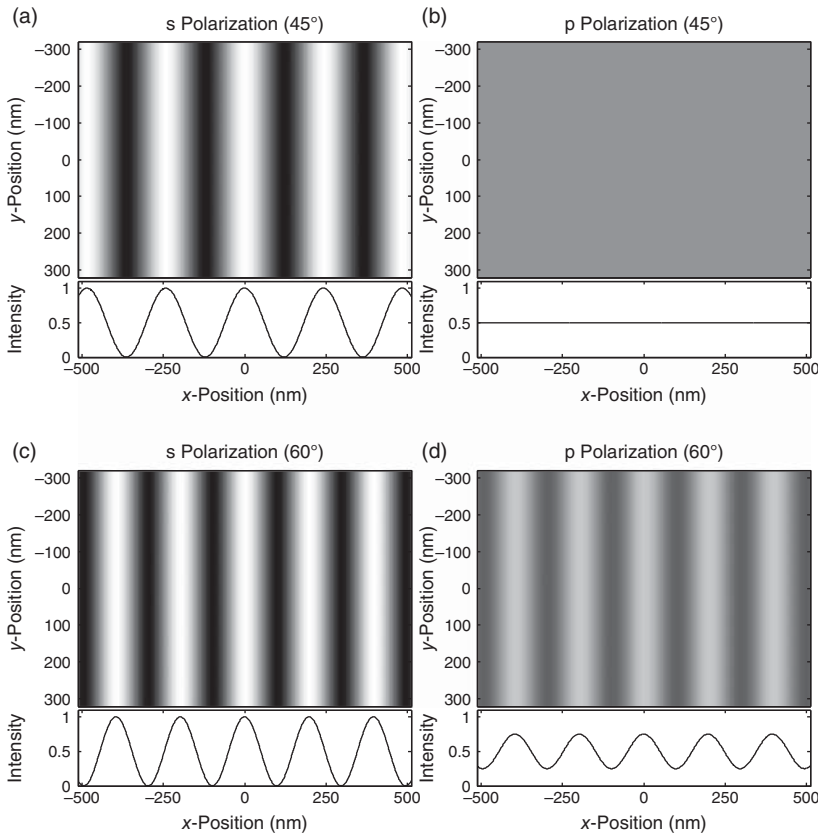
Figure 9.8 (a–d) Illumination pattern (top) and the corresponding intensity distribution (bottom) in the object plane for perpendicular (s) and parallel (p) polarization at different angles.

and a lower signal-to-noise-ratio as the number of copies would be higher. The zero-order diffraction (undiffracted beam) can optionally be blocked in order to apply two-beam interference; the use of zero, plus, and minus first order leads to the case of three-beam interference.

The phase (i.e., position) of the interference pattern in the object plane can be shifted by moving the diffraction grating in the intermediate image plane. To change the orientation of the pattern's modulation, the grating can be rotated around the optical axis.

Alternatively, a 2D grating can be applied to generate a pattern with modulation along multiple axes in the object plane, as noted in the previous section.

When an SLM is used, the pattern can be shifted and rotated by displaying different gratings on the SLM. Scientific SLMs usually consist of an array of liquid crystals to modify the polarization and/or phase of light individually for the separate pixels (a conventional liquid crystal display (LCD) is an SLM, too).

A fast SLM exhibits speed advantages over a solid grating and is also more versatile because the grating's lattice spacing can be easily adjusted to the used
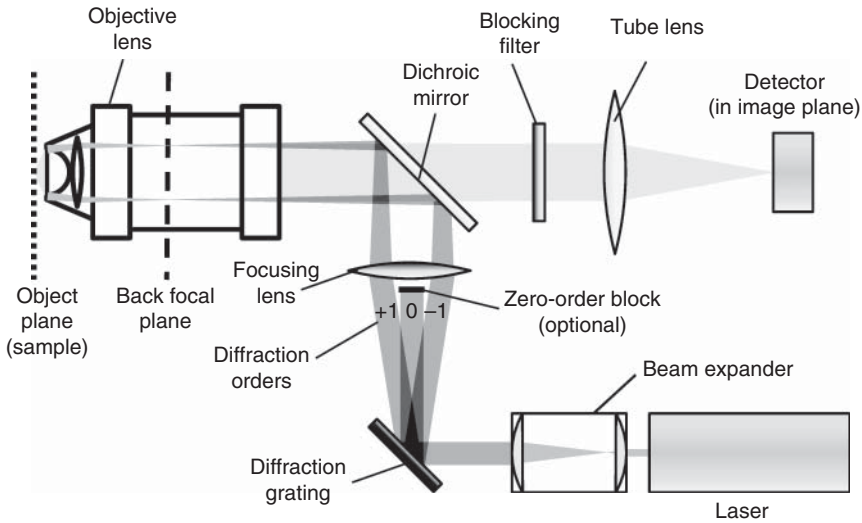
Figure 9.9 Schematic of a grating-based SIM setup. The excitation beam (dark gray) is diffracted by a grating into multiple orders. The imaging path is shown in light gray. Usually, only the zero- and first-order diffraction beams enter the objective lens. Here, the zero order can be optionally blocked by a low-frequency aperture located in front of the focusing lens to switch between three- and two-beam interference.

wavelength. Nonetheless, a solid physical grating has certain advantages over the use of an SLM. Less intensity is lost and the phase of the excitation light is less affected by spatially varying phase errors when passing through the grating, which leads to a stronger modulation of the intensity pattern in the object plane.

A different approach is to use an interferometric setup to generate the coherent beams and channel them toward the objective. A particular setup applying an interferometer [16] (Figure 9.10) is based on a Twyman–Green interferometer, which is a special case of a Michelson interferometer applying a collimated, widened beam. The used interferometer consists of a beam-splitting cube and two opposing mirrors.

This setup is based on an inversely applied, specially designed microscope. The excitation laser beam is directed to a 50% beam-splitting cube (Figure 9.10, cube A), positioned at the focal point of the focusing lens. Half of the beam is reflected by 90°, and the other half passes through the cube without any change in direction. The resulting two beams are then reflected with mirrors by 180° back into the cube. After the light passes through the beam splitter, again, two beams, each at one-fourth intensity, are generated, two of which leave the cube channeled toward the focusing lens. If the beam-splitting cube is rotated around the axis perpendicular to the table by an angle θ, one beam is deflected by 2θ and the other beam is deflected by -2θ. Thus, the interference pattern can be adjusted by rotating the beam splitter. The beams pass through the focusing lens and are then deflected by a dichromatic beam splitter toward the objective. After passing through the focusing lens and objective, the interference of the two beams in the object plane leads to a sinusoidal pattern with modulation parallel to the object
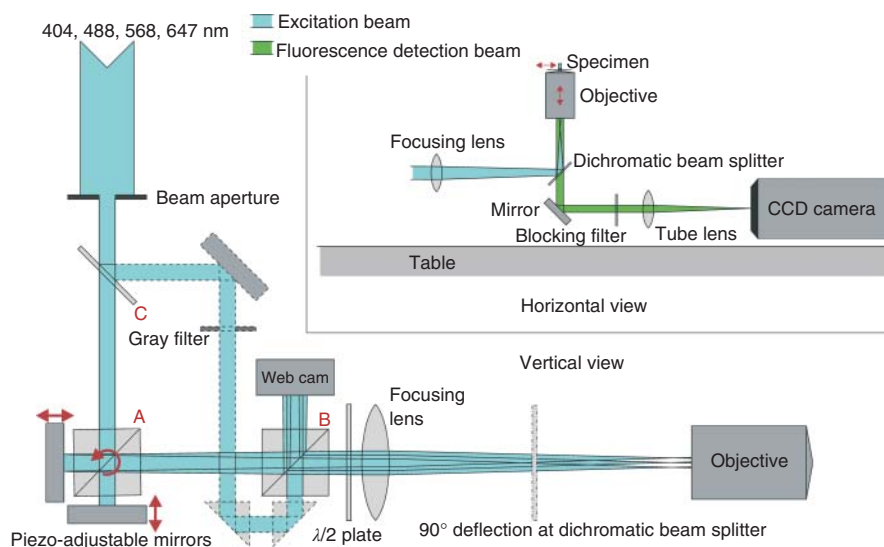
Figure 9.10 Interferometer setup for SIM. The schematic is simplified. The excitation beams are deflected by 90° onto the vertically applied objective by a dichromatic beam splitter. The deflection is not shown to improve visibility. The detection path is shown only in the horizontal view. The elements shown in dashed lines are used for the optional three-beam interference mode. The objects labeled with A, B, and C are beam splitters. The arrows indicate movable elements. (Reprinted from Best *et al*. [16], ©2011, with permission from Elsevier.)

plane. The orientation of the modulation can be changed by rotating the beam splitter around an axis parallel to the ground and perpendicular to the previous rotation axis. It is therefore possible to generate sinusoidal interference with arbitrary period and direction, which makes it possible to adjust the period of the pattern according to the particular task and wavelength. A webcam can be used to monitor the interference pattern directly. The microscope also offers the option to use a third beam, not deflected and positioned centrally to the two outer deflected beams, in order to generate a three-beam interference pattern. The beam splitter extracting the central beam (C) is located in the beam line before the other splitters. The phase of the pattern can be altered by shifting the relative phases of the separate beams. To accomplish this accurately and quickly, piezo-actuators are attached to the mirrors facing the rotatable beam-splitting cube (A).

9.3 Spatially Modulated Illumination (SMI) Microscopy

9.3.1 Overview

SMI is a microscopy method that can be used for precise size measurements of small fluorescent objects in the direction of the optical axis.

In SIM, the excitation light comes from one objective lens, and the interference pattern is spanned along the focal plane (e.g., x–y plane), whereas in SMI microscopy two counter-propagating waves from two opposing objective lenses

are used (Figure 9.11). The specimen is located between the two objectives, where the two beams form a standing wave pattern. Here, the interference pattern occurs only along the optical axis (z-direction).

Because the two beams are counter-propagating, the period of the interference pattern fringe distance d is very small (i.e., it has a high frequency). Analogous to SIM, the finer the pattern, the higher the resolution. When the resulting OTF is considered (Figure 9.12b), as in Figures 9.3 and 9.5 for SIM, in the SMI case, copies of the OTF appear shifted far in the z-direction of spatial frequencies k_z. The OTF copies have no overlap with the widefield OTF in the center, which means that the supported frequency region of the resulting OTF is not continuously interconnected. Even though information of very high-resolution frequencies in the axial direction (dashed structures in Figure 9.12b) is transmitted by the microscope, information from large frequency regions in between is not accessible.

As a consequence, the generation of high-resolution images free of artifacts, as done by SIM, is not possible by this method because large fractions of the object's moderately high-resolution information get lost.
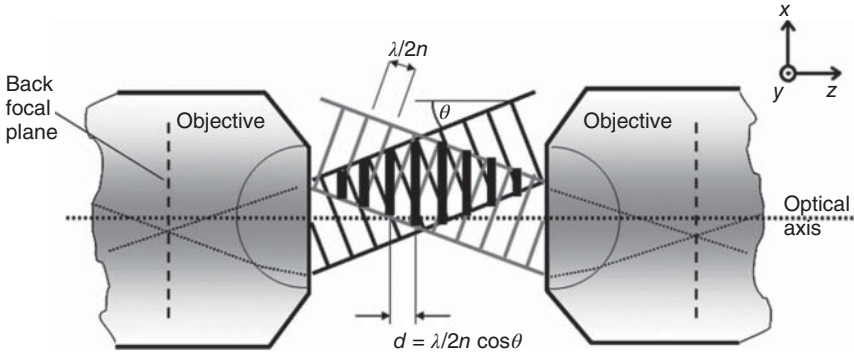
Figure 9.11 SMI setup. Two coherent light beams propagate through two opposing objectives and interfere at the object plane with a fringe distance d.
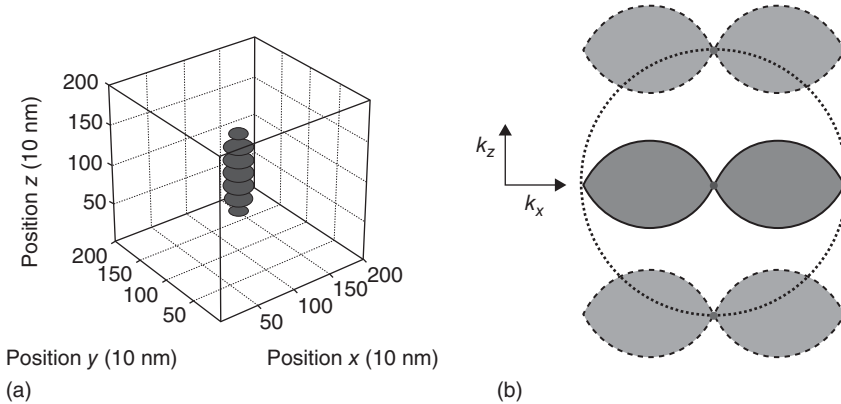

Figure 9.12 (a) Simulated SMI-PSF and (b) the corresponding OTF. While in structured illumination microscopy (SIM) the intensity is usually modulated along the optical plane, in SMI the intensity is typically modulated along the axial direction.
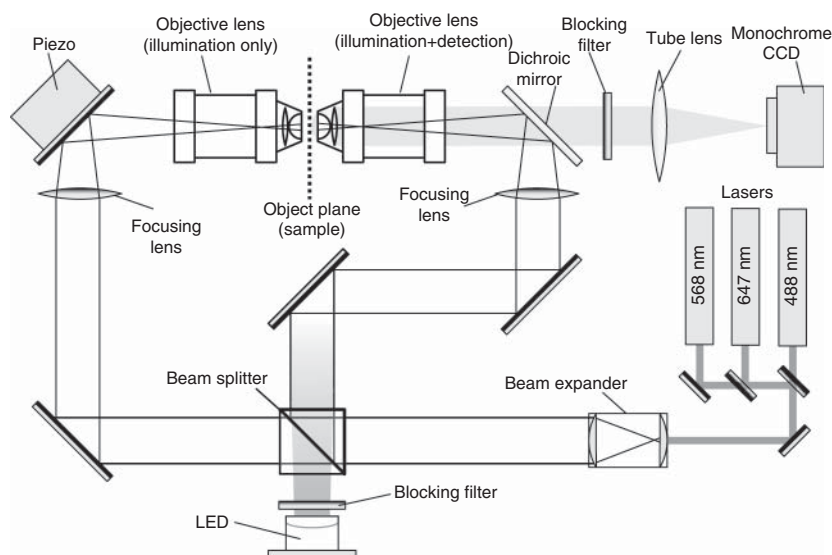
Figure 9.13 Horizontal SMI setup with three different laser sources, one LED for common transmitted light illumination, and one monochrome charge-coupled device (CCD) camera.

Therefore, *a priori* knowledge concerning the analyzed specimen is necessary in order to use SMI microscopy [17]. However, measurements of size and position along the optical axis can be done for small objects with a precision far beyond the diffraction limit – typically 40 nm – with this method.

9.3.2 SMI Setup

A typical SMI setup is shown in Figure 9.13. In order to generate two coherent and collimated beams, a collimated laser beam is divided using a beam splitter. Each beam passes through an additional lens for each objective, where the focal plane of the lens is located in the back focal plane of the objective. This converts the objective and the focusing lens into a collimator. With this optical setup, an interference pattern of sinusoidal shape along the optical axis can be generated between the objective lenses. The sample is placed between the objective lenses and can be moved along the optical axis through the interference pattern. The detection, which is similar to conventional widefield fluorescence detection, is realized by only one objective lens, which is used in conjunction with a dichroic mirror to separate the excitation light from the fluorescence signal. During image acquisition, the object is moved in precise axial steps (e.g., each 20 or 30 nm) through the standing wave field. At each step, a fluorescence image is registered [18].

9.3.3 Excitation Light Distribution

The fringe period of the standing wave located in the object plane depends on the excitation wavelength λ, the refractive index n of the sample and the

slide, as well as a possible tilting angle θ of the beams relative to the optical axis (Figure 9.11).

In the following, the mathematical expression for the intensity distribution is derived.

Two counter-propagating coherent electromagnetic waves E_l and E_r interfere in the focal region. It is assumed that both beams have the same amplitude A and that both beams might be rotated around the y-axis by an angle θ. The beam passing through the right objective (Figure 9.13) has a phase delay ϕ relative to the left beam. The result is a periodic standing wave field E_s with an intensity distribution I_s.

The calculation of the intensity distribution of the SMI interference pattern can be derived from the equation for the pattern of a two-beam interference SIM (Eq. (9.33)):

$$I = I_0(1 + \mathbf{p}_l\mathbf{p}_r \cos[(\mathbf{k}_l - \mathbf{k}_r)\mathbf{r} + \phi]) \tag{9.35}$$

In the SMI case (Figure 9.11), the wave vectors of the two beams are given by

$$\mathbf{k}_l = \begin{pmatrix} \sin\theta \\ 0 \\ \cos\theta \end{pmatrix} k \tag{9.36}$$

$$\mathbf{k}_r = \begin{pmatrix} \sin\theta \\ 0 \\ -\cos\theta \end{pmatrix} k \tag{9.37}$$

where k is the absolute value of the wave vector $\mathbf{k}$.

$$k = |\mathbf{k}| = \frac{2\pi}{\lambda} \tag{9.38}$$

The polarization is considered to be parallel to the y-axis (s polarization):

$$\mathbf{p}_l = \mathbf{p}_r = \begin{pmatrix} 0 \\ 1 \\ 0 \end{pmatrix} \tag{9.39}$$

The intensity becomes

$$I = I_0(1 + \cos[2\cos\theta kz + \phi]) \tag{9.40}$$

The illumination pattern can be phase-shifted by changing the optical path length difference ϕ of the interferometer. k, the norm of the wave vector $\mathbf{k}$, is expanded by the refractive index factor n of the medium, as the wavelength of light is inversely proportional to n:

$$\lambda = \frac{\lambda_0}{n} \tag{9.41}$$

$$\Rightarrow k = k_0 n; \quad k_0 = \frac{2\pi}{\lambda_0} \tag{9.42}$$

The grating distance G_{SMI} of the pattern in the z-direction can be derived from Eq. (9.35) by

$$(\mathbf{k}_{\mathrm{l}} - \mathbf{k}_{\mathrm{r}}) = \begin{pmatrix} 0 \\ 0 \\ G_{\mathrm{SMI}} \end{pmatrix} = 2kG_{\mathrm{SMI}} \cos\theta = 2\pi \tag{9.43}$$

$$G_{\mathrm{SMI}} = \frac{\lambda_0}{2n\cos\theta} \tag{9.44}$$

This means that for samples with a thickness larger than G_{SMI}, multiple interference fringes are located inside this volume and, as a result, no unique phase position might be distinguishable. Several maxima of the illumination pattern might be located in the depth of the sample simultaneously, irrespective of the actual phase of the pattern.

For a well-aligned system with a tilting angle below 10° ($\cos\theta \approx 1$), the cosine term in Eq. (9.44) can be neglected. A fringe period is obtained that is proportional to the vacuum wavelength λ_0 divided by 2 times the refractive index. Using an immersion medium with a high refractive index, n will be roughly 1.5. In this case, the fringe distance is λ divided by 3. Therefore, an excitation wavelength of 488 nm results in a fringe distance of ~163 nm. This means that the intensity profile of the excitation pattern has a maximum every 163 nm. When this value is compared with the axial depth of focus (~600 nm for an NA 1.4 objective lens), it can be seen that there is more than one intensity maximum within the focal depth (Figure 9.12a). Hence, it is possible to achieve information from the high-resolution region beyond the classical resolution limit. The approach is described in the following sections.

9.3.4 Object Size Estimation with SMI Microscopy

There are two major effects that occur when moving the sample through the focus of the detection objective lens. On one hand, the detected intensity is modulated by the interference of the excitation pattern while the modulation contrast depends on the object size. On the other hand, there is a variation of intensity between objects in the focus and outside the focus.

The analysis of SMI data is primarily based on these two effects. The axial PSF of a widefield microscope along the optical axis is given by a sinc^2 function (Chapter 2). As a result of two-beam interference, the excitation intensity distribution is given by a $\cos^2$ function (Equation 9.10).

When the illumination pattern is kept fixed to the object plane and a point-like object is moved along the z-direction, two effects superpose. The illumination intensity will vary sinusoidally because of the illumination pattern, and the image of the object will move through the focus. As a result, the illumination pattern and the widefield PSF are multiplied to form the resulting spatially modulated illumination-point spread function (SMI-PSF) (Figure 9.14). Figure 9.12 shows the 3D SMI-PSF and the corresponding OTF.

The axial SMI-PSF shows as the envelope the sinc^2 function, which is modulated by a $\cos^2$ interference pattern. In this example of an infinitely small point-like object, the modulation contrast $R = 1$. The modulation contrast R is defined as follows:

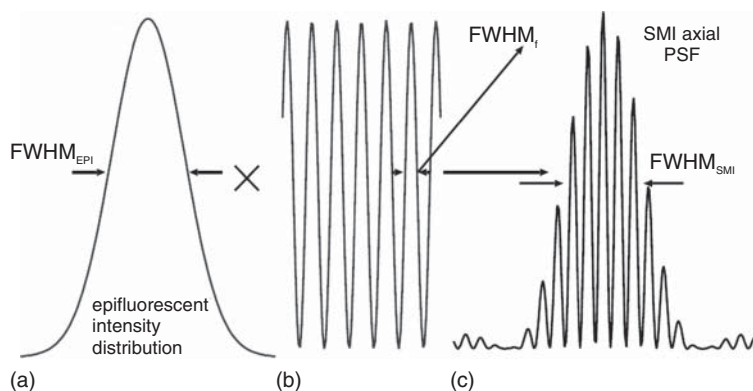$$R = \frac{I_{\max} - I_{\min}}{I_{\max}} \tag{9.45}$$

Figure 9.14 Axial detection PSF (a), excitation pattern (b), and resulting axial SMI point spread function (c).

where I_{max} and I_{min} represent the maximum and minimum intensity values of the inner and outer SMI-PSF envelopes, respectively. In other words, the detected axial intensity distribution (AID) is an overlap of the small fringes from the excitation light modulation and the envelope function from the axial detection of the objective lens [19] (see also Figure 9.14):

$$\text{AID} = \left(\frac{\sin(k_1 z)}{k_1 z} \right)^2 \times (a_1 \times \cos^2(k_2 z) + a_2) \tag{9.46}$$

In this equation, k_1 represents the FWHM of the envelope function, k_2 is the wave vector of the standing wave field, a_1 represents the modulation strength, and a_2 defines the modulation contrast. For simplification, additional phase-offset values and nonmodulated parameters are neglected in this formula.

When, instead of a tiny point object, a larger object is imaged, the modulation contrast is smaller than 1 and varies with the object's size and geometry [20–22]. When analyzing biological nanostructures, it is often convenient to assume a spherical geometry. Figure 9.15 shows the modulation contrast R as a function of the diameter of a spherical object. Obviously, the modulation contrast graph is not bijective. For a given modulation contrast, there might be several solutions for the size of the object. The modulation contrast for spherical objects is 0 for certain object sizes (240 and 415 nm for 488 nm excitation wavelength). This means
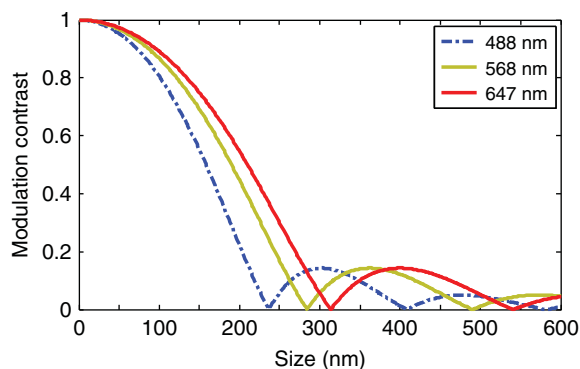

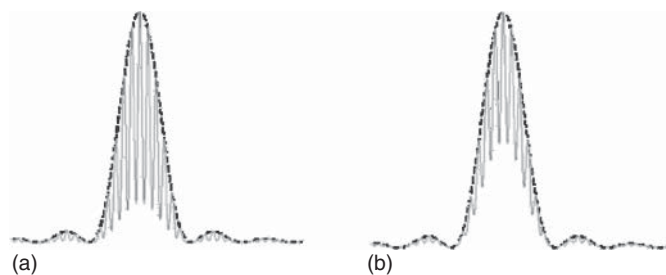**Figure 9.15** Modulation contrast function for different wavelengths.

(a)   (b)

Figure 9.16 Simulation of the expected intensity distribution for a small object ((a) ø 50 nm at 488 nm excitation wavelength) and a larger object ((b) ø 150 nm at 488 nm excitation wavelength) under object scanning condition with an SMI microscope.

that the emitted intensity does not vary when the illumination pattern is shifted through the specimen for these object sizes.

If the application of SMI is constrained to the case of a modulation contrast beyond 0.18, which corresponds to an object size of roughly 200 nm, the relation is bijective and therefore can be used for size determinations. Above this size limit, conventional microscopy can be used to determine the object's size. The smallest diameter is limited by the shape of the modulation contrast function and the amount of detected photons. Typically, even sizes of around 40 nm can be measured by SMI with high precision.

The graphs in Figure 9.15 were calculated for the case of a spherical object with a homogeneous fluorophore density distribution [23]. If the object is small compared to the interference pattern, the detected fluorescence signal is similar to that in Figure 9.16a.

When the diameter of the object increases (Figure 9.16b), the modulation depth decreases, but the fringe distance stays the same and the envelope function also roughly stays the same. In the extreme case, the modulation contrast R will disappear when the object diameter becomes much larger than the fringe distance. By the use of the simulated modulation contrast graph (Figure 9.15), it is possible to extract a value for the diameter of a diffraction-limited object from the measured modulation contrast. It is important to keep in mind that this value is a calculated value under some assumptions – especially the geometry of the object has to be defined *a priori* – and that this value may differ from the "true" size if the assumptions are incorrect.

9.4 Application of Patterned Techniques

Patterned techniques have become an important tool in microscopic analysis of biomedical subjects. Today, almost every major microscope manufacturer provides a SIM system.

In this paragraph, some brief examples for applications of patterned techniques are discussed. One of the many applications of SIM is the analysis of autofluorescent structures in tissue of the eye. Degradation of the retinal pigment epithelium (RPE) is responsible for the age-related macular degeneration

(AMD), the main reason for blindness in the developed world in the elderly population. This disease, in which vision in the macula (the region of sharpest sight) is progressively lost, is linked to excessive aggregations of autofluorescent compounds in the RPE cells. RPE is a cell monolayer between the retina and the choroid. It has essential functions in sustaining the vision process. The compound called *lipofuscin* accumulating in the RPE cells is autofluorescent, which makes it easily detectable by fluorescence imaging without the need for additional labeling.

The images presented here have been generated with an interferometric SIM setup [16]. Paraffin sections of human retinal tissue have been cut, deparaffined, and prepared on object slides [24]. The specimens were analyzed using three different excitation wavelengths (488, 568, and 647 nm).The use of different excitation wavelengths showed a spatially varying composition of the fluorescent granules.

When comparing the acquired SIM images with the standard widefield data, the considerable improvement of the former is apparent (Figures 9.17 and 9.18). Not only is the contrast greatly improved but also is the optical resolution
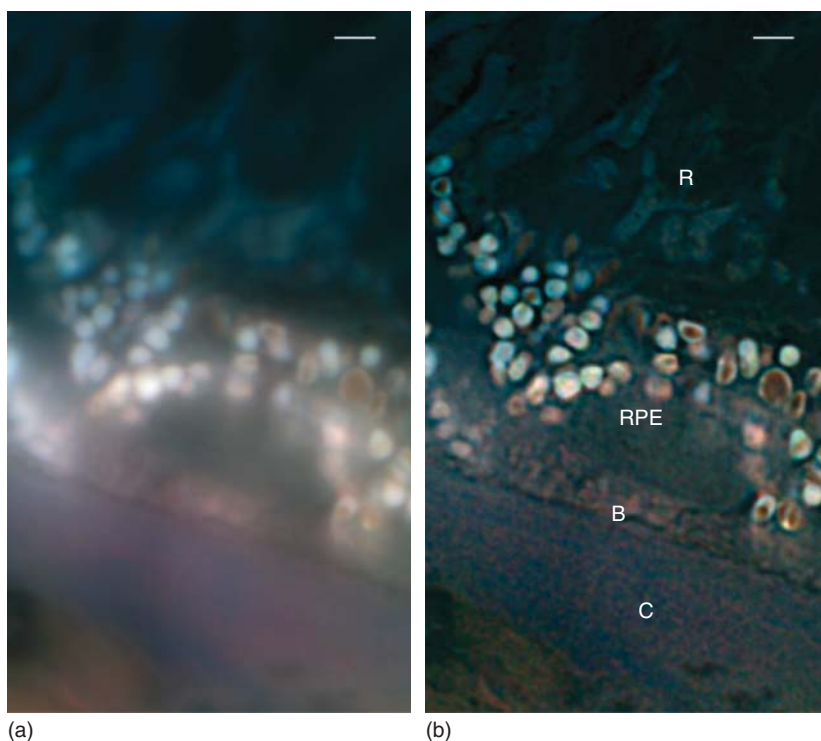
(a)　　　　　　　　　　　　　　　　　(b)

Figure 9.17 Multicolor SIM image of retinal pigment epithelium (RPE). The colors red, green, and blue represent the signal for 647, 568, and 488 nm excitation, respectively. The SIM image (b) shows more details and less out-of-focus light than the widefield image (a). The background of each channel is subtracted, and each channel is stretched to full dynamic range. The Bruch membrane (B) is located between the choroid (C) and the RPE. On the top of the image, endings of retinal rod cells (R) can be seen. The scale bar is 2 μm [16]. (Reprinted from Best et al. [16], with permission from Elsevier.)
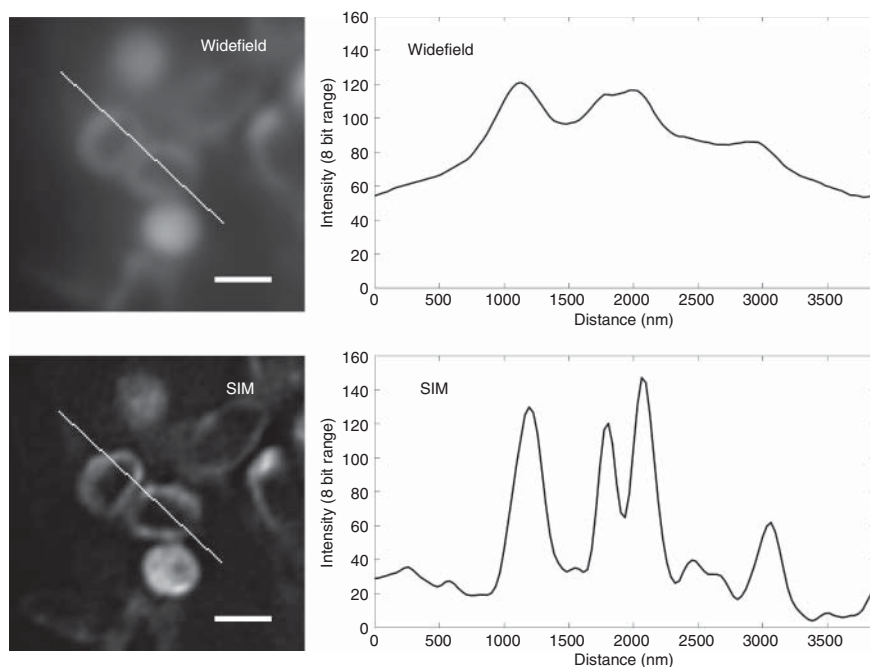
Figure 9.18 Image analysis: widefield versus structured illumination microscopy. The specimen was excited with 488 nm light. The scale bar is 1 μm. (Reprinted from [16], with permission from Elsevier.)

enhanced by a factor of 1.6–1.7 depending on the wavelength. Thus, previously nonresolvable details can be discovered. Figure 9.18 shows the intensity along a line through structures in RPE cells below 488 nm excitation each in a widefield image and the corresponding structured illumination image. The gray value (intensity) of both images was normalized to full 8-bit range, and the background intensity was subtracted.

The improvement of contrast in the SIM image is apparent by the efficient suppression of out-of-focus light, resulting in higher dynamic range in the examined region.

The lateral resolution enhancement allows additional details to be seen (e.g., the two circular structures in the center of the image can clearly be separated in the SIM image). The suppression of out-of-focus light allows the generation of 3D images. SIM images at several axial focal positions are acquired, and the resulting high-resolution data is combined into a 3D dataset. The acquisition speed of SIM is sufficient to allow super-resolution imaging of living cells, as shown in Figure 9.19.

The other microscopy technique treated in this chapter, namely the more specialized method SMI, is suitable for analysis of small nanostructures in biological specimens.

Baddeley *et al.* [25] showed that SMI can be used to measure the size of DNA replication foci in the nucleus of mammalian cells. For this study, both SMI and SIM have been used.
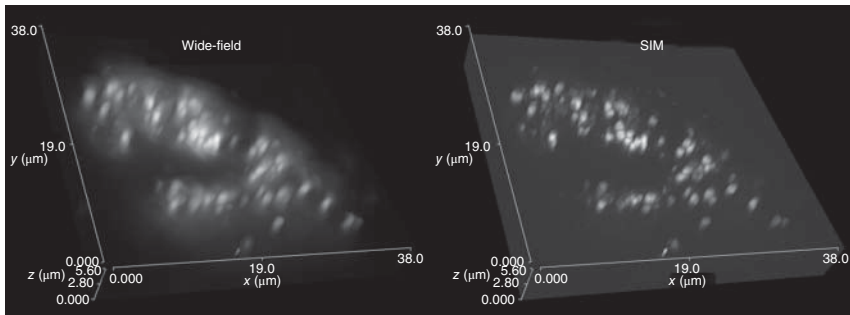
Figure 9.19 3D SIM image of autofluorescent lipofuscin granules inside of a living RPE cell.

Both methods showed an average size of 125 nm irrespective of the labeling method. Remarkably, the super-resolution methods were able to resolve three- to fivefold more distinct replication foci than previously reported. For the SMI data analysis, the data stack was first filtered for pointlike objects. For the identified objects, an axial profile was extracted, which was then analyzed with the SMI methods described in Section 9.3.4 to determine their accurate size. A spherical geometry was assumed for the single replication foci (Figure 9.20).
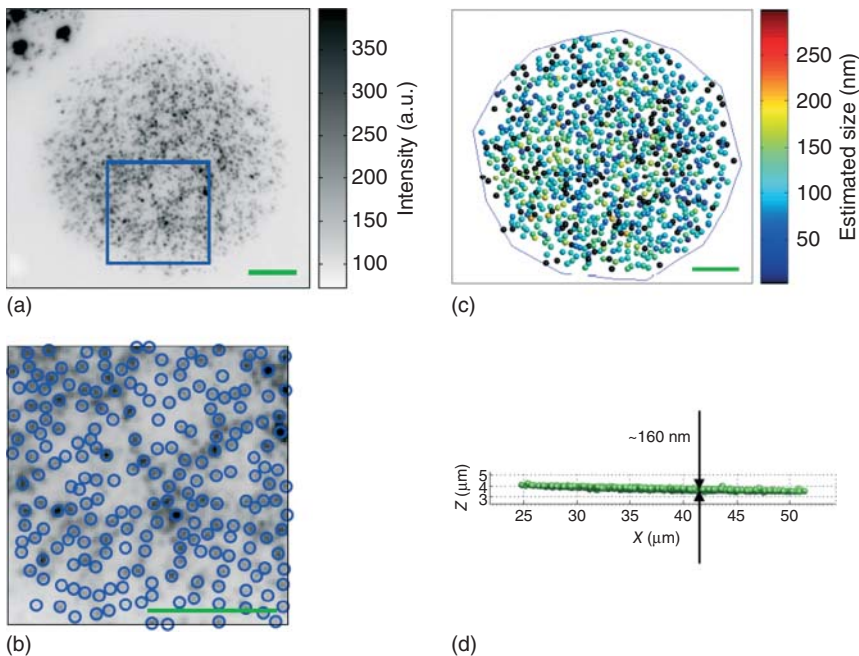

Figure 9.20 SMI analysis of DNA replication foci. Panel (b) shows thresholded foci from the raw data (a). Panel (c) shows the size of the foci (the black ones had to be ignored because of insufficient signal level or a size outside of the effective range). Panel (d) shows the axial position of the analyzed foci [25]. (Baddeley *et al*. 2010 [25]. Reproduced with permission of Oxford University Press.)

9.5 Conclusion

Interference techniques deliver increased optical resolution albeit at the cost of increased acquisition time and higher irradiance. The main benefit of these techniques compared to other super-resolution techniques is that no special requirements for the applied fluorochromes are necessary. No photoswitching or nonlinear effects are necessary to increase the resolution. The approach is based solely on the change in the intensity distribution of the excitation light compared to standard fluorescence microscopy. However, super-resolution methods based on nonlinear effects have the intrinsic advantage of even higher resolution than SIM (theoretically unlimited).

Often, the ease of use makes SIM the high-resolution method of choice for many biomedical applications. In contrast to most other high-resolution techniques, SIM allows living cell analysis because of relatively short acquisition times and low excitation intensities. Compared to conventional confocal microscopy, SIM delivers a superior image quality and optical resolution at a comparable applicability. Even though linear patterned techniques cannot compete directly with localization methods for single molecules (Chapter 8) in terms of positioning accuracy, they can deliver complementary information. When both methods are combined, high structural resolution, on one hand, and high localization accuracy, on the other, can be realized [26].

9.6 Summary

Fluorescence microscopy techniques using patterned illumination light offer the opportunity to extract high-resolution object information beyond the conventional resolution limit. Especially the SIM technique, where laterally modulated illumination through one objective lens is used, has evolved to become an important tool for high-resolution imaging in biomedical research. Because of the interplay of the illumination pattern with the object's spatial frequencies, a resolution improvement by a factor of 2 is possible in SIM. In this chapter, we provided a fundamental mathematical description of this method and presented different variations of the SIM setups. The secondary focus of this chapter was on the less common method of SMI, where two opposing objective lenses are used to generate a high-frequency interference pattern along the optical axis. The SMI method is used to measure the size of nanostructures with great precision. At the end of the chapter, we provided a brief description of exemplary biological applications for the two patterned illumination methods.

Acknowledgments

SIM. We gratefully appreciate the support of the members of the group of Christoph Cremer, especially the help of Margund Bach.

References

1 Rayleigh, L. (1896) On the theory of optical images, with special reference to the microscope. *Philos. Mag. J. Sci.*, **42** (255), 167–195.

2 Cremer, C. and Cremer, T. (1978) Considerations on a laser-scanning-microscope with high resolution and depth of field. *Microsc. Acta*, **81** (1), 31–44.

3 Hell, S. and Stelzer, E.H. (1992) Fundamental improvement of resolution with a 4Pi-confocal fluorescence microscope using two-photon excitation. *Opt. Commun.*, **93** (5), 277–282.

4 Hell, S.W., Lindek, S., Cremer, C., and Stelzer, E.H. (1994) Confocal microscopy with an increased detection aperture: type-B 4Pi confocal microscopy. *Opt. Lett.*, **19** (3), 222–224.

5 Hänninen, P.E., Hell, S.W., Salo, J., Soini, E., and Cremer, C. (1995) Two-photon excitation 4Pi confocal microscope: enhanced axial resolution microscope for biological research. *Appl. Phys. Lett.*, **66**, 1698–1700.

6 Gustafsson, M.G. (2000) Surpassing the lateral resolution limit by a factor of two using structured illumination microscopy. *J. Microsc.*, **198** (2), 82–87.

7 Heintzmann, R. and Cremer, C.G. (1999) Laterally modulated excitation microscopy: improvement of resolution by using a diffraction grating. SPIE BiOS Europe'98, pp. 185–196, http://proceedings.spiedigitallibrary.org/ proceeding.aspx?articleid=972650 (accessed 10 May 2013).

8 Abbe, E. (1873) Beiträge zur Theorie des Mikroskops und der mikroskopis-chen Wahrnehmung. *Arch. Mikrosk. Anat.*, **9** (1), 413–418.

9 Heintzmann, R., Jovin, T.M., and Cremer, C. (2002) Saturated patterned exci-tation microscopy – a concept for optical resolution improvement. *J. Opt. Soc. Am. A Opt. Image Sci. Vision*, **19** (8), 1599–1609.

10 Gustafsson, M.G. (2005) Nonlinear structured-illumination microscopy: wide-field fluorescence imaging with theoretically unlimited resolution. *Proc. Natl. Acad. Sci. U.S.A.*, **102** (37), 13081–13086.

11 Heintzmann, R. and Ficz, G. (2006) Breaking the resolution limit in light microscopy. *Briefings Funct. Genomics Proteomics*, **5** (4), 289–301.

12 Pawley, J.B. (ed.) (2006) *Handbook of Biological Confocal Microscopy*, Springer, Boston, MA, http://link.springer.com/10.1007/978-0-387-45524-2 (accessed 22 February 2016).

13 Karadaglić, D. and Wilson, T. (2008) Image formation in structured illumina-tion wide-field fluorescence microscopy. *Micron*, **39** (7), 808–818.

14 Hirvonen, L., Mandula, O., Wicker, K., and Heintzmann, R. (2008) Structured illumination microscopy using photoswitchable fluorescent proteins. *Proc. SPIE*, **6861**, 68610L. doi: 10.1117/12.763021

15 Kner, P., Chhun, B.B., Griffis, E.R., Winoto, L., and Gustafsson, M.G.L. (2009) Super-resolution video microscopy of live cells by structured illumination. *Nat. Methods*, **6** (5), 339–342.

16 Best, G., Amberger, R., Baddeley, D., Ach, T., Dithmar, S., Heintzmann, R. *et al.* (2011) Structured illumination microscopy of autofluorescent aggregations in human tissue. *Micron*, **42** (4), 330–335.

17 Spöri, U., Failla, A.V., and Cremer, C. (2004) Superresolution size determination in fluorescence microscopy: a comparison between spatially modulated illumination and confocal laser scanning microscopy. *J. Appl. Phys.*, **95** (12), 8436–8443.

18 Reymann, J., Baddeley, D., Gunkel, M., Lemmer, P., Stadter, W., Jegou, T. *et al.* (2008) High-precision structural analysis of subnuclear complexes in fixed and live cells via spatially modulated illumination (SMI) microscopy. *Chromosome Res.*, **16** (3), 367–382.

19 Schneider, B., Upmann, I., Kirsten, I., Bradl, J., Hausmann, M., and Cremer, C. (1999) A dual-laser, spatially modulated illumination fluorescence microscope. *Microsc. Anal.*, **57** (1), 5–7.

20 Failla, A.V., Spoeri, U., Albrecht, B., Kroll, A., and Cremer, C. (2002) Nanosizing of fluorescent objects by spatially modulated illumination microscopy. *Appl. Opt.*, **41** (34), 7275–7283.

21 Albrecht, B., Failla, A.V., Heintzmann, R., and Cremer, C. (2001) Spatially modulated illumination microscopy: online visualization of intensity distribution and prediction of nanometer precision of axial distance measurements by computer simulations. *J. Biomed. Opt.*, **6** (3), 292–299.

22 Wagner, C., Spöri, U., and Cremer, C. (2005) High-precision SMI microscopy size measurements by simultaneous frequency domain reconstruction of the axial point spread function. *Optik*, **116** (1), 15–21.

23 Wagner, C., Hildenbrand, G., Spöri, U., and Cremer, C. (2006) Beyond nanosizing: an approach to shape analysis of fluorescent nanostructures by SMI-microscopy. *Optik*, **117** (1), 26–32.

24 Ach, T., Best, G., Ruppenstein, M., Amberger, R., Cremer, C., and Dithmar, S. (2010) Hochauflösende Fluoreszenzmikroskopie des retinalen Pigmentepithels mittels strukturierter Beleuchtung. *Ophthalmologe*, **107** (11), 1037–1042.

25 Baddeley, D., Chagin, V.O., Schermelleh, L., Martin, S., Pombo, A., Carlton, P.M. *et al.* (2010) Measurement of replication structures at the nanometer scale using super-resolution light microscopy. *Nucleic Acids Res.*, **38** (2), e8.

26 Rossberger, S., Best, G., Baddeley, D., Heintzmann, R., Birk, U., Dithmar, S. *et al.* (2013) Combination of structured illumination and single molecule localization microscopy in one setup. *J. Opt.*, **15** (9), 094003.